



Stress state of Koyna intraplate seismic region, India, from focal mechanism data

Journal:	<i>Geophysical Journal International</i>
Manuscript ID:	Draft
Manuscript Type:	Research Paper
Date Submitted by the Author:	
Complete List of Authors:	Manglik, Ajay; National Geophysical Research Institute Rebetsky, Yu.; Schmidt United Institute of Physics of Earth Davulluri, Srinagesh; National Geophysical Research Institute, Seismological Observatory Thiagarajan, S.; National Geophysical Research Institute
Keywords:	Seismicity and tectonics < SEISMOLOGY, Intra-plate processes < TECTONOPHYSICS, Asia < GEOGRAPHIC LOCATION

Stress state of Koyna intraplate seismic region, India, from focal mechanism data

A. Manglik^{1*}, Yu. Rebetsky², D. Srinagesh¹, and S. Thiagarajan¹

1. National Geophysical Research Institute, Uppal Road, Hyderabad 500606, INDIA.

2. Schmidt United Institute of Physics of Earth, 10 B. Gruzinskaya Street 123995 Moscow, RUSSIA.

*** Address for correspondence:**

Dr. Ajay Manglik
National Geophysical Research Institute
Uppal Road, Hyderabad – 500 606
INDIA.

Tel. : +91-40-23434684

Fax. : +91-40-23434651

Email: ajay@ngri.res.in

Version : October 20, 2009

Running Title : Stress state of Koyna intraplate seismic region

Keywords : Seismicity and tectonics, Intra-plate processes, Asia

Abstract

Koyna intraplate seismic region (KSR) in the Deccan Volcanic Province of western India has experienced a large number of reservoir triggered earthquakes including 17 events of magnitude ≥ 5 over a period of four decades. Continuation of intraplate seismicity over such a long duration offers an extensive data set of earthquake parameters to study the spatio-temporal variations in the seismicity of the region. The focal mechanism solutions, although limited in number and available mainly for moderate magnitude earthquakes, can be used to quantify the prevailing stress state in the region. In the present study, we perform stress inversion analysis to quantify the stress state of this region using published focal mechanisms of earthquakes of magnitude 3.9-6.7, occurred during 1967-2005. The results suggest that region has small cohesive strength of 9.6 MPa and the maximum shear stress varies from 19.2 MPa to 163 MPa with the average value of 67.2 MPa. The analysis also indicates the presence of lateral compression and high pore fluid pressure in the region. The coupled effect of high fluid pressure, compressive forces and low cohesive strength of the rocks could possibly provide an explanation for the region being critically stressed and causing recurrent seismic activity in KSR for over four decades.

Introduction

Koyna intraplate seismic region in the Deccan Volcanic Province (DVP) of western India [Figure 1] is the unique intraplate region in the world where reservoir associated seismicity has continued for over 40 years ever since the impoundment of the Sivajisagar reservoir in 1961 [Gupta 2002]. Warna reservoir was impounded in 1985 and is located to the south of Koyna leading to an increase in intense seismic activity which is continuing till date. Together Koyna-Warna region has experienced more than 1,00,000 earthquakes of small magnitude which includes 17 earthquakes of magnitude ≥ 5 which have occurred during this period [Gupta, 2002]. The largest earthquake of magnitude 6.3 occurred in this region on 1967.12.10 [Gupta et al., 1969], more than five years after the impoundment of the reservoir. Detailed spatial analysis of vast amount of earthquake data revealed the presence of several seismogenic crustal blocks in the region lying between Koyna and Warna rivers [Talwani, 1997]. Three broad seismicity trends, a NNE trend near the Koyna reservoir, another trend 20 km west of the reservoir and a NW trend cutting through these two, were identified based on the above analysis of clustering of epicenters. More recent studies using a dense network of digital seismometers and precise time control have further refined the seismicity trends and

revealed three distinct trends, one NNE-SSW near Koyna reservoir, and the other two nearly parallel NNW-SSE trends near Warna reservoir [Rai et al., 1999]. Based on these results, the whole region has been sub-divided into Koyna Seismic Zone (KSZ) and Warna Seismic Zone (WSZ). However, in the present paper we consider these two zones together as Koyna Seismic Region (KSR).

Continuation of moderate seismicity for such a long time and its link to the reservoir water level changes suggests that the region is critically stressed due to tectonic causes [Rai et al., 1999; Gahalaut et al., 2004] and water level changes provide necessary trigger for the earthquakes [Gupta, 2002]. Various geophysical techniques have been used to map the subsurface structure of KSR in order to provide better structural control for earthquake studies. These include deep seismic sounding (DSS) studies along two E–W traverses [Kaila et al., 1981], deep electrical sounding [Kailasam et al., 1976], seismic tomography [Rai et al., 1999; Srinagesh et al., 2000], gravity studies [Krishna Brahmam and Negi, 1973], and MT studies [Gokarn et al., 2003; Sarma et al., 2004]. DSS results bring out the presence of steep dip faults cutting across the entire crust in this region [Kaila et al., 1981]. A further re-analysis of these data identified low velocity layers (LVL) in the upper as well as lower crust at depths of 6–11 km and 26–28 km [Krishna et al., 1997]. Talwani [1997] correlated the earthquakes to the LVL at 6-11 km depth. In contrast, seismic tomography results inferred a high seismic velocity block reaching to shallow depths from the lower crust in the region of seismicity [Srinagesh et al., 2000]. Bouguer gravity anomaly over KSR was earlier interpreted in terms the presence of a sub-trap rift-valley structure [Krishna Brahmam and Negi, 1973]. However, recent MT results ruled out such a possibility and showed that the KSR appears as a moderately conducting structure bounded on both the sides by high resistive blocks [Sarma et al., 2004]. This conductive feature is never-the-less confined to the upper 4-5 km of the crust even though the seismicity extends down to the depth of 15 km. Thus, KSR also presents a range of contrasting results.

There are only very limited stress data available from the Indian shield region. These data are mainly obtained by focal mechanism solutions of intraplate earthquakes. For KSR, the direction of maximum compressive stress, obtained by focal mechanism data of moderate magnitude Koyna earthquakes, is mainly N-S [Reinecker et al., 2005]. Since KSR has experienced a large number of earthquakes over a period of four decades, it offers an extensive data set to study the spatial-temporal variations in the stress levels for better

understanding of the causative mechanism. However, focal mechanism data of only a limited number of earthquakes are available. In the present study, we perform stress inversion analysis to calculate the stress state of KSR using a small data set consisting of published focal mechanisms of earthquakes of magnitude 3.9-6.7 occurred during 1967-2005.

Focal Mechanism Data

Despite the occurrence of a large number of small-to-moderate magnitude earthquakes in KSR focal mechanism solutions for a small number of earthquakes are available. Talwani [1997] presented a compilation of focal mechanisms of moderate magnitude earthquakes till 1997 along with detailed discussion on various focal mechanisms available for the largest magnitude 1967.12.10 earthquake. Focal mechanisms for the earthquakes during 1997-2005 are from Harvard CMT catalog [<http://www.seismology.harvard.edu>] and are given in Table 1. Events 3-10 in Table 1 are composite fault plane solutions obtained by Gupta et al. [1980] and for events 11-19 are from Talwani [1997]. The details of location, origin time, depth and magnitude, if not available in respective publications, have been included from the NEIC catalog [<http://www.usgs.gov>]. In some cases, both the nodal planes of the published focal mechanisms were not consistent and therefore, revised focal mechanisms of Gahalaut [personal communication] for these events have been used (shown in bold letters in Table 1). Focal mechanisms of all the events used in the present analysis are shown in Figure 2.

Stress Inversion Analysis

We use the Cataclastic Analysis Method (CAM) of earthquake focal mechanisms [Rebetsky, 1999, 2003] which gives the directions of principal stresses as well as the maximum shear stress and effective isotropic pressure (isotropic pressure in solid rocks minus pore fluid pressure). The CAM is also applicable for the estimation of paleo-stresses from geological structural data (slip on faults). This method involves four steps. In the first step, principal axes of stress and seismotectonic strain tensors are calculated. During this stage groups of uniform samples are created from initial structural kinematic data (SKD) such as focal mechanism data [Rebetsky, 1999]. For the calculation of parameters of seismotectonic strain tensor we have assumed that the increment of residual strain $d\epsilon_{ij}^l$ caused by each earthquake ($l=1,2,\dots,N$; N is the number of earthquakes in a set of uniform samples) is comprised of deformations determined by the area of fault plane (Ω^l) and the amplitude of average

displacement (D^l) along it, averaged over the volume of elastic discharge area (V^l) of the earthquake, i.e.

$$d\varepsilon_{ij}^l = \frac{\Omega^l D^l}{2V^l} (n_i^l r_j^l + n_j^l r_i^l); \quad (i, j = 1, 2, 3), \quad (1)$$

where n_i and r_i are direction cosines of the vectors normal to the fault plane and displacement along the fault plane, respectively [Rebetsky, 1999]. For seismic data, we can not choose n_i and r_i from earthquake source mechanism and this selection is arbitrary. A uniform sample of earthquake mechanisms thus selected represents a crustal domain subject to quasi-homogeneous deformation under the predicted stress. For a set of uniform samples the seismotectonic strain tensor can be determined as:

$$S_{ij} = \sum_{l=1}^N d\varepsilon_{ij}^l. \quad (2)$$

In the framework of CAM eq. (1) and (2) may be re-written as:

$$S_{ij} = 0.5 \gamma \sum_{l=1}^N (n_i^l r_j^l + n_j^l r_i^l), \quad \text{where } \gamma = \Omega^l D^l / V^l \approx D^l / L^l = \text{constant}. \quad (3)$$

Here, the effective shear strain γ characterizes the elastic strain drop of earthquakes and for analyzing sub-region (domain of stress reconstruction for a set of N earthquakes) it is assumed as constant ($L = A + B \cdot 10^{1.24 + 0.8M_b - 5}$ km is the characteristic size of an earthquake focal length; A and B are the coefficients governing the change in stress and M_b is the magnitude).

For the calculation of the principal axes of a stress tensor σ_i ($\sigma_1 \geq \sigma_2 \geq \sigma_3$ with tension as +ve) CAM uses energy constraint of the plasticity theory. This constraint requires a decrease in the internal elastic energy after each earthquake, i.e.

$$\sigma_{ij} d\varepsilon_{ij}^l \geq 0 \quad l = 1, 2, \dots, N. \quad (4)$$

This equation constrains the deviation of the angle between the vectors of shear stress and displacement on a fault plane (this angle should be smaller than 90°). Under this constraint, we can get an equation for the orientation of the principal stresses as:

$$n_1^l r_1^l \geq n_2^l r_2^l \geq n_3^l r_3^l \text{ for } n_i^l r_i^l = 0 \quad l=1,2,\dots,N. \quad (5)$$

Details of this method are discussed in [Rebetsky \[1997, 1999, 2003\]](#). Eq.(5) is used to construct uniform samples of earthquake focal mechanisms. A uniform sample of earthquake focal mechanisms thus selected represents a crustal domain subject to quasi-homogeneous deformation under the predicted stress. This equation also allows calculation of variations in the directions of principal stress axes. Parameters of stress ellipsoid are calculated on the basis of these variations and using the principle of plasticity theory about maximum dissipation of internal energy accumulated by elastic strain ($\sigma_{ij} S_{ij}$). At the end of the first stage, we get three Euler angles for the calculation of direction cosine of the principal stress axes and the Lode-Nadai coefficient μ_σ (a coefficient representing the shape of the deviatoric stress ellipsoid. $\mu_\sigma = -1$: uni-axial extension to $\mu_\sigma = +1$: uni-axial compression, and $\mu_\sigma = 0$: pure shear).

The second stage of CAM is based on the analysis of brittle behavior of rocks. Here, the maximum stress state corresponds to the maximum value of cohesion τ_f representing the effective strength limit of rock [[Figure 3](#)]. This can be expressed as:

$$\tau_n + k_f (\sigma_{nn} + p_{fl}) = \tau_f \text{ for } \tau_n > 0 \text{ and } \sigma_{nn} \leq 0, \quad (6)$$

where σ_{nn} and τ_n are normal and shear stress, respectively, for the internal friction coefficient k_f of rock and p_{fl} is the pore fluid pressure (compression of isotropic pressure is +ve i.e. $p_{fl} \geq 0$). For the fault plane of an earthquake l we can similarly express the stress state as

$$\tau_n^l + k_s^l (\sigma_{nn}^l + p_{fl}) = \tau_s^l \text{ for } \tau_n^l > 0 \text{ and } \sigma_{nn}^l \leq 0, \quad (7)$$

where σ_{nn}^l and τ_n^l are normal and shear stress, respectively, on the fault plane of the earthquake l forming the uniform samples, τ_s^l is the surface cohesion ($0 \leq \tau_s^l \leq \tau_f$) and k_s^l is the static surface friction coefficient of preexisting fault. For simplicity, we assume that $k_s^l = k_f$. Thus, a line with zero cohesion represents the minimum bound on the stress for brittle failure and the region between the two lines in the Mohr diagram [Figure 3] is the area of brittle failure on preexisting faults.

After the first stage of stress analysis, we can calculate reduced stress ($\tilde{\sigma}_{nn}, \tilde{\tau}_n$) on fault planes with arbitrary orientation on the basis of following expression:

$$\begin{aligned}\tilde{\sigma}_{nn} &= (\sigma_{nn} + p) / \tau = (1 - \mu_\sigma)(n_1^l)^2 - (1 + \mu_\sigma)(n_3^l)^2, \\ \tilde{\tau}_n &= \tilde{\sigma}_{nt} = \sigma_{nt} / \tau = (1 - \mu_\sigma)n_1^l t_1^l - (1 + \mu_\sigma)n_3^l t_3^l,\end{aligned}\quad (8)$$

where $\tau = (\sigma_1 - \sigma_3)/2$, $p = -(\sigma_1 + \sigma_2 + \sigma_3)/3$. Here n_i^l and t_i^l ($i = 1, 2, 3$) are direction cosines of normal to arbitrary orientated fault plane and shear stress direction of this plane in the coordinate system of predicted principal stress axes; p and τ are unknown isotropic pressure and maximum shear stress. Note from Eq.(5) the angle between vector t_i^l and vector r_i^l (displacement vector on the fault plane) should be positive.

Eq.(7) can be used to select the fault plane from the double couple focal mechanism nodal planes (n_i^l and s_i^l) of an earthquake assuming that the focal plane is the one that allows the largest stress release. In the framework CAM this condition is represented by

$$\tau_n^l + k_s^l \sigma_{nn}^l > \tau_s^l + k_s^l \sigma_{ss}^l. \quad (9)$$

Reduced stresses for each uniform sample of earthquakes allow plotting of pairs of σ_{nn} and τ_n in the Mohr diagram to construct big limiting Mohr circle and obtain minimum friction resistance corresponding to $\tau_s^l = 0$ in the framework of CAM. Thus, the reduced stress state at a point can be calculated by using eq.(8) and angle α_B can be estimated from the Mohr diagram [Figure 3]. Using these values relative effective pressure and the maximum shear stress can be calculated by the following expression:

$$\begin{aligned} \left\langle \frac{p_{eff}}{\tau_f} \right\rangle &= \frac{(\tilde{\tau}_n^K + k_s \tilde{\sigma}_{nn}^K)}{k_s [\operatorname{cosec}(2\alpha_B) - k_s \mu_\sigma / 3 - (\tilde{\tau}_n^K + k_s \tilde{\sigma}_{nn}^K)]}, \\ \left\langle \frac{\tau}{\tau_f} \right\rangle &= \frac{1}{\operatorname{cosec}(2\alpha_B) - k_s \mu_\sigma / 3 - (\tilde{\tau}_n^K + k_s \tilde{\sigma}_{nn}^K)}, \end{aligned} \quad (10)$$

where $2\alpha_B = \arctan\left(\frac{1}{k_s}\right)$ and $p_{eff} = p - p_{fl}$. Second step of the stress analysis gives stress estimates normalized to an unknown internal cohesion τ_f of rocks.

In the third stage of CAM, the internal cohesion is determined by using independent information of stress drop during a strong earthquake [Rebetsky and Marinin, 2006a,b]. After the second stage of CAM the stress drop $\Delta\tau_n$ normalized to τ_f can be related to the fault normal effective stress $(\sigma_{nn} + p_{fl})$ as:

$$\left\langle \frac{\Delta\tau_n}{\tau_f} \right\rangle = 1 - (k_s - k_k) \left\langle \frac{\sigma_{nn} + p_{fl}}{\tau_f} \right\rangle, \quad (11)$$

where right side of this equation can be calculated on the basis of the results of the first and the second stage of stress analysis as

$$\left\langle \frac{\sigma_{nn} + p_{fl}}{\tau_f} \right\rangle = - \left\langle \frac{p_{eff}}{\tau_f} \right\rangle + \left[(1 - \mu_\sigma)(l_{n1})^2 - (1 + \mu_\sigma)(l_{n3})^2 \right] \left\langle \frac{\tau}{\tau_f} \right\rangle. \quad (12)$$

Here, k_s and k_k are the static and kinematic friction coefficient ($k_k \leq k_s$), respectively. Eq.(11) gives the value of stress drop. In the present analysis, we assume that $k_k = 0.5$ and $k_s = 0.6$.

Alternatively, the stress drop, $\Delta\tau_n$, can be independently estimated from the seismic moment and energy of seismic radiation. Thus, knowing the value of the stress drop $\Delta\tau_n$ from earthquake data it is possible to obtain the value of the cohesion τ_f by using the following expression:

$$\tau_f = \Delta\tau_n \left\langle \frac{\Delta\tau_n}{\tau_f} \right\rangle^{-1}. \quad (13)$$

Once τ_f is known, we can estimate the absolute values of the maximum shear stress and effective isotropic pressure from eq.(10).

In the forth step of CAM separation of isotropic pressure and fluid pressure can be carried out by assuming the vertical stress to be equal to the weight of the column of rock [Sibson, 1974]

$$\sigma_{zz} = -\rho g(h + h_t), \quad (14)$$

where ρ and g are density and gravity acceleration and h , h_t are the depth of the point at which the stress is calculated and topography, respectively. Using eq.(14) and reduced stress we can write an equation for the calculation of pressure as:

$$p = \rho g h + \left\langle \frac{\tau}{\tau_f} \right\rangle \tilde{\sigma}_{zz} \tau_f, \quad (15)$$

where $\tilde{\sigma}_{zz} = (\sigma_{zz} + p)/\tau = [(1 - \mu_\sigma)(z_1)^2 - (1 + \mu_\sigma)(z_3)^2]$. Here, z_i ($i = 1, 2, 3$) are direction cosines of the zenith vector in the coordinate system of principal stress axes.

Results

We performed stress inversion of the focal mechanisms given in Table 1 and shown in figure. 1. The focal depths are distributed over 4 – 15 km depths. There are three events with focal depths in the range of 25 to 35 km but these depths are unlikely for this region. Since the number of available focal mechanisms is very small to extract the sets of homogeneous samples (stage 1 of the analysis), we have assigned a focal depth of 15 km to all these events.

The results of the first stage of stress reconstruction for this data set are shown in figure 4. Here, horizontal projections of the directions of principal deviatoric stresses $\sigma_1 + p$ (maximum extension) and $\sigma_3 + p$ (maximum compression) are shown as blue and red lines, respectively [Figure 4a]. Maximum deviatoric extension axis has ENE plunge for the

northern part of the region and west plunge for the southern part of the region. In the central part, these axes are sub-horizontal and their strike have NE orientation. Maximum deviatoric compression has sub-horizontal orientation for the northern part of the region and sub-vertical for other parts of the region. Orientation of these axes allows separation of sub-regions based on different stress regime [Figure 4b]: horizontal extension (blue), horizontal compression (red), strike slip (yellow). The distribution of the Lode-Nadai coefficient (μ_σ) is shown in figure 4c. This figure shows three distinct stress regimes: uni-axial extension (blue color), uni-axial compression (red color), simple shear (yellow color). The variation in μ_σ suggests that the KSZ region has mainly simple shear to uni-axial compression deformation whereas WSZ has more complex deformation mechanism. The junction of the KSZ and WSZ shows extensional deformation mechanism.

The results at the end of the second stage of stress reconstruction by CAM are shown in figure 5. At this stage, we have calculated effective pressure p_{eff} and maximum shear stress τ , both normalized to an unknown cohesion τ_f , by performing Mohr diagrams analysis for each homogeneous sample of earthquakes. The results show the variations in the maximum shear stress in the range of 2-17 with the mean values of 7.0 [Figure 5a]. The effective pressure follows the pattern of the shear stress variations and has a positive correlation with it [Figure 5b]. It varies in the range of 3-38. The regions of large shear stress coincide with the regions of large effective pressure. Incidentally, the seismicity is correlated with the regions of low effective pressure and shear stress.

In the third stage of stress analysis, we have calculated effective cohesion (τ_f) of rocks using available estimates of the stress drop for earthquakes. Some estimates of the stress drop from the seismic moment are available for KSZ. Talwani [1997] compiled various estimates of the stress drop ($\Delta\tau_n$) of the main earthquake of 1967.12.10 (M=6.3). These estimates vary in the range of 0.6 – 23.8 MPa. An estimate of 23.8 MPa was obtained from the displacement spectra of strong ground motion seismograms. Mandal et al. [1998] estimated the stress drop to be in the range of 0.03 to 19 MPa for the earthquakes in this region ranging in magnitude between 1.5 and 4.7. In their study, the maximum stress drop of 19 MPa was obtained for a 4.7 magnitude earthquake. Ajay Kumar et al. [2006] also obtained a similar stress drop of 19 MPa for another earthquake of 5.1 magnitude and attributed this to the presence of competent material within the source volume. Based on these studies, we have taken 20 MPa as an

average value of the stress drop for this region. On the basis of the results of the first and the second stage of stress reconstruction we have calculated normalized stress drop for both nodal planes of the main earthquake (1967.12.10) by taking the stress data of the region near the hypocenter. The obtained normalized stress drop $\langle \Delta \tau_n / \tau_f \rangle$ is 1.43 for the first nodal plane (strike = 217.0, dip= 72.0, slip= 4.0) whereas it is 2.09 for the second nodal plane (strike= 126.0, dip= 84.0, slip= 162.0).

Using the criterion given by eq.(9), we have selected the second nodal plane as the fault plane for this earthquake and the value of 2.09 as the corresponding stress drop. Once the value of the stress drop is fixed, we can calculate the value of the effective cohesion using eq.(13) which comes out to be 9.6 MPa. It means that the maximum shear stress for this region varies from 19.2 MPa to 163 MPa with the mean value of about 67.2 MPa.

Figure 6 shows the ratio of the tectonic pressure to the lithostatic pressure p / p_{lt} and pore fluid pressure to the lithostatic pressure p_f / p_{lt} , respectively. The value of p / p_{lt} varies between 1.02 - 1.17 and has an average value of 1.08, indicating that the region is experiencing an additional compression (possible lateral) over the lithostatic pressure [Figure 6a]. The magnitude of this additional average compression at a given depth can be estimated from the lithostatic pressure at that depth. For example, assuming the density of rocks as 2700 kg/m³ the average compression at 15 km depth is about 32 MPa. Similarly, the ratio of pore fluid pressure to the lithostatic pressure varies between 0.31-0.96 [Figure 6b] with a large area having higher pore fluid pressure. The seismogenic volume and the region of high fluid pressure are coincident, indicating that the fluid pressure is playing a significant role in weakening the system of faults in KSR.

Conclusion

Stress inversion analysis of focal mechanism solutions in KSR for the earthquakes during 1967-2005 distinctly brings out that the cohesive strength of the rocks is 9.6 MPa and the maximum shear stress varies between 19.2 to 163 MPa, with lower values coinciding with the region of seismic activity. Further, the region of lower maximum shear stress is conspicuous with high fluid pressure reaching almost to the lithostatic levels. The analysis also reveals the presence of compressive forces acting additionally in this region. The coupled effect of high fluid pressure, compressive forces and low cohesive strength of the rocks could possibly

provide an explanation for the region being critically stressed and causing recurrent seismic activity in KSR for over four decades.

Acknowledgement

This work has been supported by Department of Science and Technology, India, and Russian Academy of Sciences, Russia, under the framework of Indo-Russian programme of collaboration (ILTP). Authors are grateful to the Russian and Indian coordinators of the programme, and to the Director, NGRI, Hyderabad, and Director General, IPE, Moscow, for their support. We thank Dr. V.K. Gahalaut for providing revised focal mechanisms of some of the earthquakes used in the analysis.

References

- Ajay Kumar B., Ramana D.V., Patanjali Kumar Ch., Swaroopa Rani V., Shekar M., Srinagesh D., and Chadha R.K., 2006. Estimation of source parameters for 14 March 2005 earthquake of Koyna-Warna region. *Curr. Sci.*, 91, 526-530.
- Dziewonski A.M., Ekstrom G., Franzen J.E., and Woodhouse J.H., 1988. Global seismicity of 1980: Centroid moment tensor solutions for 515 earthquakes. *Phys. Earth Planet Int.*, 50, 127-154.
- Gahalaut V.K., Kaplana, and Singh S.K., 2004. Fault interaction and earthquake triggering in the Koyna-Warna region, India. *Geophys. Res. Lett.*, 31m L11614, doi: 10.1029/2004GL019818.
- Gokarn S.G., Gupta G., Rao C.K. and Selvaraj J. 2003. Some interesting observations on the tectonics in the Deccan Volcanic Province observed from magnetotelluric studies. *J. Virtual Explorer* 12, 55-65.
- Gupta H.K., 2002. A review of recent studies of triggered earthquakes by artificial water reservoirs with special emphasis on earthquakes in Koyna, India. *Earth Science Reviews*, 58, 279-310.
- Gupta H.K., Narain H., Rastogi B.K., Mohan I., 1969. A study of the Koyna earthquake of December 10, 1967. *Bull. Seismol. Soc. Am.*, 59, 1149-1162.
- Gupta H.K., Ram Krishna Rao C.V., Rastogi B.K., and Bhatia S.C., 1980. An investigation of earthquakes in Koyna region, Maharashtra, for the period October 1973 through December 1976. *Bull. Seismol. Soc. Am.*, 70, 1833-1847.
- Kaila K.L., Reddy P.R., Dixit M.M., Lazrenko, 1981. Deep crustal structure at Koyna, Maharashtra indicated by deep seismic soundings. *J. Geol. Soc. India*, 22, 1-16.
- Kailasam L.N., Reddy A.G.B., Rao J., Sathyamurthy K., Murthy B.S.R., 1976. Deep electrical resistivity soundings in Deccan trap region. *Curr. Sci.*, 45, 4-16.
- Krishna V.G., Kaila K.L., and Reddy P.R., 1997. Low velocity layers in the subcrustal lithosphere beneath the Deccan Traps region of western India. *Pnys. Earth Planet. Int.*, 67, 288-302.
- Krishna Brahmam N. and Negi J.G., 1973. Rift valleys beneath the Deccan Trap (India). *Geophys. Res. Bull.* 11, 207-237.

1
2
3
4
5
6
7
8
9
10
11
12
13
14
15
16
17
18
19
20
21
22
23
24
25
26
27
28
29
30
31
32
33
34
35
36
37
38
39
40
41
42
43
44
45
46
47
48
49
50
51
52
53
54
55
56
57
58
59
60

Lee W.H.K. and Raleigh C.B., 1969. Fault-plane Solution of the Koyna (India) Earthquake. *Nature*, 223, 172-173.

Mandal P., Rastogi B.K., and Sarma C.S.P., 1998. Source parameters of Koyna earthquake, India. *Bull. Seismol. Soc. Am.*, 88, 833–842.

Rai S.S., Singh S.K., Rajagopal Sarma P.V.S.S., Srinagesh D., Reddy K.N.S., Prakasam K.S., Satyanarayana Y., 1999. What triggers Koyna region earthquakes? Preliminary results from seismic tomography digital array. *Earth Planet. Sci.*, 108, 1–14.

Rao B.S.R., Prakasa Rao, T.K.S., and Rao V.S., 1975. Focal mechanism study of an aftershock in the Koyna region of Maharashtra state, India. *Pure Appl. Geophys.*, 113, 483-488.

Rebetsky Yu.L., 1997. Reconstruction of tectonic stresses and seismotectonic strains: methodical fundamentals, current stress field of Southeastern Asia and Oceania. *Dokl. Akad. Nauk*, 354, 101-104.

Rebetsky Yu.L., 1999. Methods for reconstructing tectonic stresses and seismotectonic deformations based on the modern theory of plasticity. *Dokl. Akad. Nauk*, 365, 370-373.

Rebetsky Yu.L., 2003. development of the method of cataclastic analysis of shear fractures for tectonic stress estimation. *Dokl. Akad. Nauk*, 388, 72-76.

Rebetsky Yu. L. and Marinin A.V., 2006a. Stress state of Earth's crust in the western region of Sunda subduction zone before the Sumatra-Andaman earthquake on December 26, 2004. *Dokl. Akad. Nauk*, 407, 812–815.

Rebetsky Yu. L. and Marinin A.V., 2006b. Preseismic stress field before Sumatra-Andaman earthquake of 26.12.2004. A model of metastable state of rocks. *Geol. i Geofiz.*, 47, 1173-1185.

Sarma S.V.S., Patro B.P.K., Harinarayana T., Veeraswamy K., Sastry R.S., Sarma M.V.C., 2004. A magnetotelluric (MT) study across the Koyna seismic zone, western India: evidence for block structure. *Phys. Earth Planet. Int.*, 142, 23-36.

Sibson R.H., 1974. Frictional constraints on thrust, wrench and normal faults. *Nature*, 249, 542–544.

Srinagesh D., Singh S., Reddy K.S., Prakasam K.S., Rai S.S., 2000. Evidence for high velocity in Koyna seismic zone from p-wave teleseismic imaging. *Geophys. Res. Lett.*, 27, 2737–2740.

Talwani P., 1997. Seismotectonics of the Koyna-Warna area, India. *Pure Appl. Geophys.*, 150, 511-550.

Reinecker J., Heidbach O., Tingay M., Sperner B., and Müller B., 2005. The release 2005 of the World Stress Map (www.world-stress-map.org).

List of Tables

Table 1. Focal mechanism data used in the present analysis. For some events, re-estimated focal mechanisms (marked in bold face) have been used. Where ever not available in respective publications, latitudes/longitudes have been taken from NEIC catalog. Since time accuracy up to seconds is not available for old events, we show time only up to minutes for all the events.

List of Figures

Figure 1. Map showing location of the Koyna (KSZ) and Warna (WSZ) Seismic Zones along with distribution of seismicity superimposed on topography. Black stars show the epicenters of the earthquakes used in the present analysis. Topography data are taken from GTOPO30.

Figure 2. Focal mechanisms of earthquakes used in the present analysis.

Figure 3. Mohr diagram for stress state (extension +ve). Dark gray color area is the area of possibility of brittle destruction at preexisting fault. Point B characterize a stress state for internal strength of rock, points A and C characterize fault planes with maximum deviation from the plane of internal strength of rock. Point K represents fault with minimum frictional resistance.

Figure 4. (a) Horizontal projections of directions of maximum extensional principal stress σ_1 (blue) and minimum extensional principal stress σ_3 (red), (b) stress state regime: 1– horizontal extension; 2– combination of horizontal extension and horizontal strike slip; 3– horizontal strike slip; 4– combination of horizontal compression and horizontal strike slip; 5– horizontal compression, and (c) distribution of Lode-Nadai coefficient μ_σ . Stars are epicenters of earthquakes used in the present analysis.

Figure 5. Distribution of (a) maximum shear stress τ normalized to τ_f and (b) correlation between maximum shear stress and effective pressure at the end of second stage of stress inversion analysis. Stars are epicenters of earthquakes used in the present analysis.

Figure 6. Distribution of (a) tectonic pressure to the lithostatic pressure p/p_l , and (b) pore fluid pressure to the lithostatic pressure p_f/p_l . Stars are epicenters of earthquakes used in the present analysis.

Table 1. Focal mechanism data used in the present analysis. For some events, re-estimated focal mechanisms (marked in bold face) have been used. Where ever not available in respective publication, latitudes/longitudes have been taken from NEIC catalog. Since time accuracy up to seconds is not available for old events, we show time only up to minutes for all the events.

SN	Year	MM	DD	HH	MM	Mag.	Longitude [E]	Latitude [N]	Depth [km]	Plane - 1			Plane - 2			REF
										Strike	Dip	Slip	Strike	Dip	Slip	
1	1967	12	10	22	51	6.3	73.75	17.35	10.3	217	72	4	126	84	162	1
2	1967	12	12	15	48	5	73.68	17.28	...	22	56	187	116	82	-35	2,5
3	1973	10	17	15	24	5.1	74.75	17.35	...	202	57	-7	296	84	-146	8
4	1974	02	17	14	06	4.6	73.82	17.20	6.9	5	76	-175	97	86	-15	3,5
5	1974	08	28	20	20	4.5	73.75	17.21	5.0	185	76	-6	276	84	-166	8
6	1974	11	11	15	11	4.4	73.79	17.23	6.0	346	80	-90	166	10	-90	3,5
7	1974	12	20	14	16	4.0	73.75	17.36	5.0	166	80	-90	346	10	-90	8
8	1975	12	02	07	40	4.4	73.69	17.24	...	358	80	-90	178	10	-90	3,5
9	1975	12	24	13	25	4.3	73.68	17.22	6.9	178	80	-90	358	10	-90	8
10	1976	03	14	05	16	4.7	73.75	17.24	4.0	316	40	-90	136	50	-90	3,5
11	1980	09	20	10	45	5.3	73.58	17.31	15.0	32	74	90	212	14	90	3,5
12	1993	08	28	04	26	4.9	73.67	17.17	5.0	212	74	90	32	14	90	8
13	1993	09	03	23	01	4.7	73.74	17.13	35.0	318	60	-90	138	30	-90	3,5
14	1993	10	22	01	14	4.3	73.96	17.44	33.0	138	60	-90	318	30	-90	8
15	1993	12	08	01	42	5.1	73.63	17.07	25.0	258	30	-90	78	60	-90	3,5
16	1993	12	21	10	15	4.0	73.76	17.17	...	92	70	-90	272	20	-90	8
										350	62	-156	91	70	-31	3,5
										170	62	-24	272	70	-150	8
										139	29	-111	342	63	-79	4,5,7
										165	40	-180	75	90	50	5,7
										165	40	-180	255	90	50	8
										296	90	-25	25	25	-180	5,7
										115	90	65	25	25	-180	8
										16	37	-25	135	70	-120	5,7
										16	37	-25	126	75	-124	8
										44	45	-49	173	58	-123	4,5
										2	50	-160	260	75	-40	5
										2	50	-160	259	75	-42	8

17	1994	01	22	11	12	3.8	73.75	17.18	...	319	56	135	75	65	50	5
18	1994	02	01	09	30	5.4	73.52	17.23	10.0	319	56	135	78	54	44	8
19	1994	03	01	16	07	3.7	73.78	17.19	...	45	35	-130	91	64	-105	5,7
20	2000	03	12	18	03	4.9	73.67	17.10	15.0	325	65	160	63	72	27	8
21	2000	09	05	00	32	5.4	73.85	17.37	15.0	302	56	112	86	40	61	8
22	2005	03	14	09	43	4.9	73.73	17.15	13.0	352	23	-95	176	67	-88	6,7
										354	21	-94	178	69	-89	6,7
										334	40	-118	189	55	-68	6,7

REF: 1- Lee and Raleigh (1969), 2- Rao et al. (1975), 3- Gupta et al. (1980), 4- Dziewonski et al. (1988), 5- Talwani (1997), 6- Harvard CMT catalog, 7- NEIC catalog, and 8- Gahalaut (per. comm.).

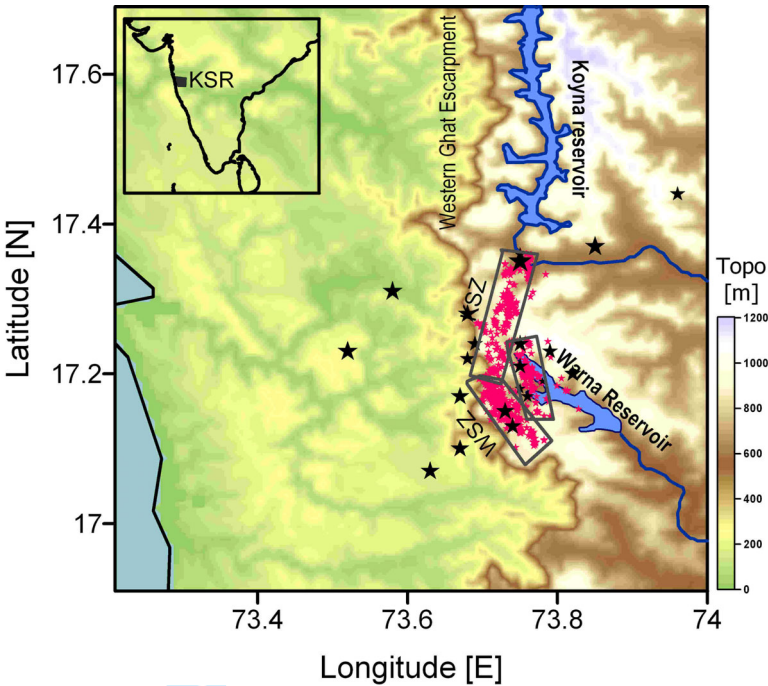


Figure 1

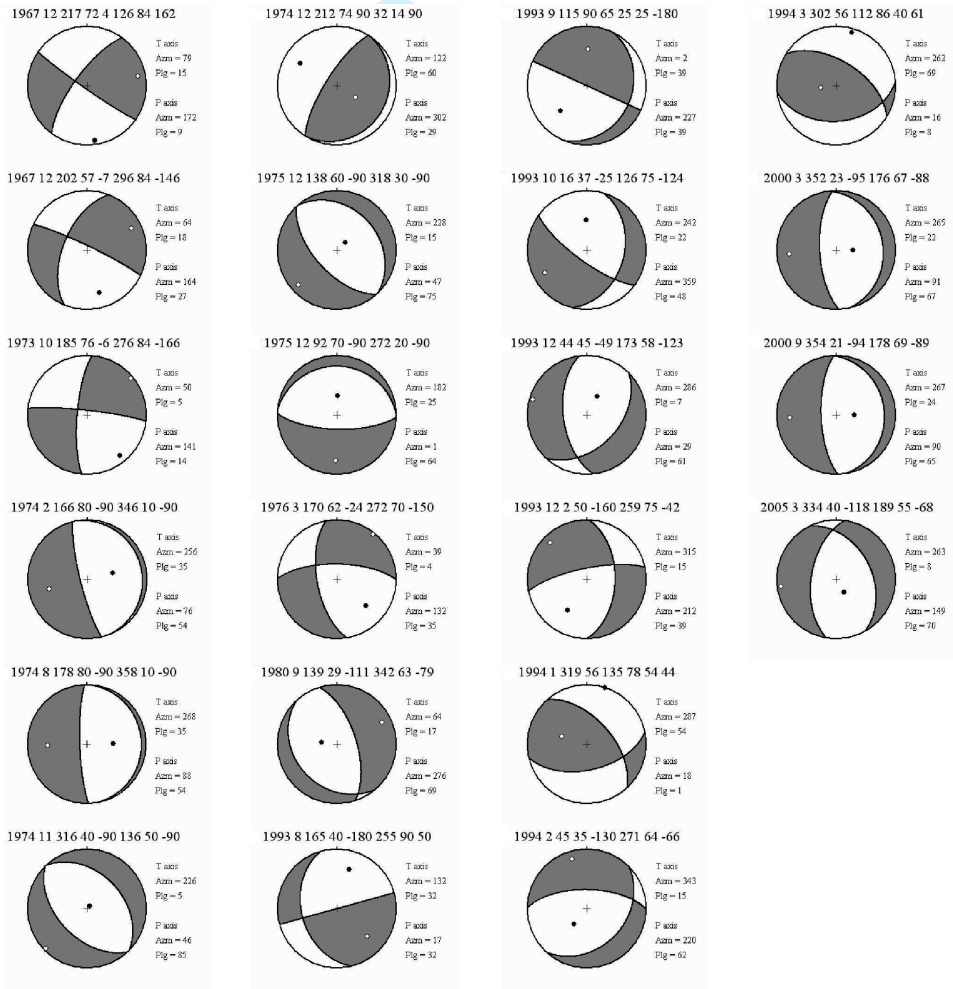


Figure 2

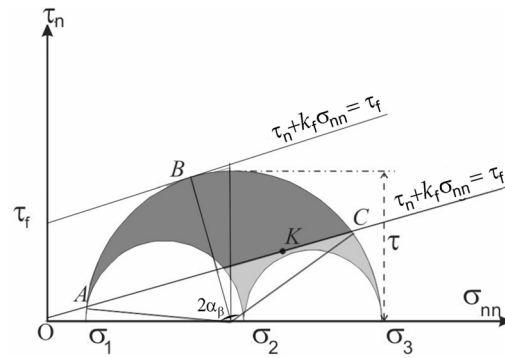


Figure 3

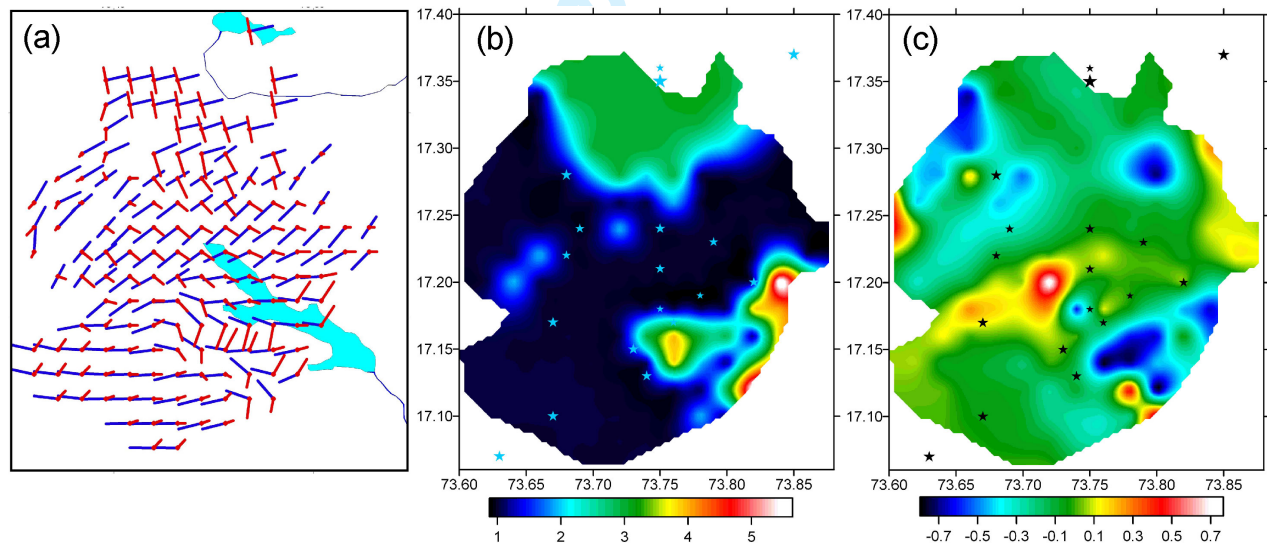


Figure 4

1
2
3
4
5
6
7
8
9
10
11
12
13
14
15
16
17
18
19
20
21
22
23
24
25
26
27
28
29
30
31
32
33
34
35
36
37
38
39
40
41
42
43
44
45
46
47
48
49
50
51
52
53
54
55
56
57
58
59
60

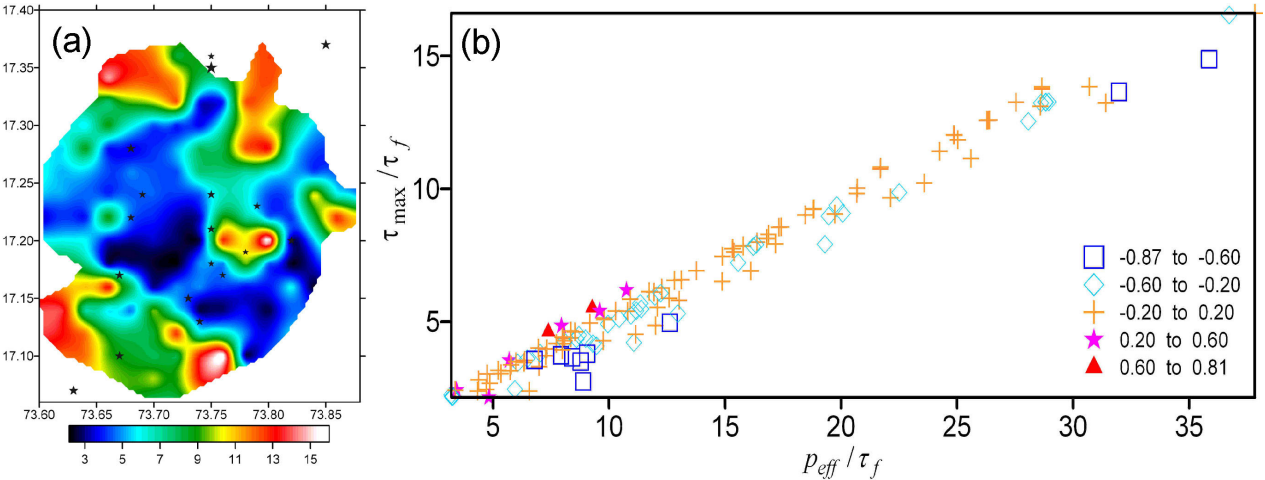


Figure 5

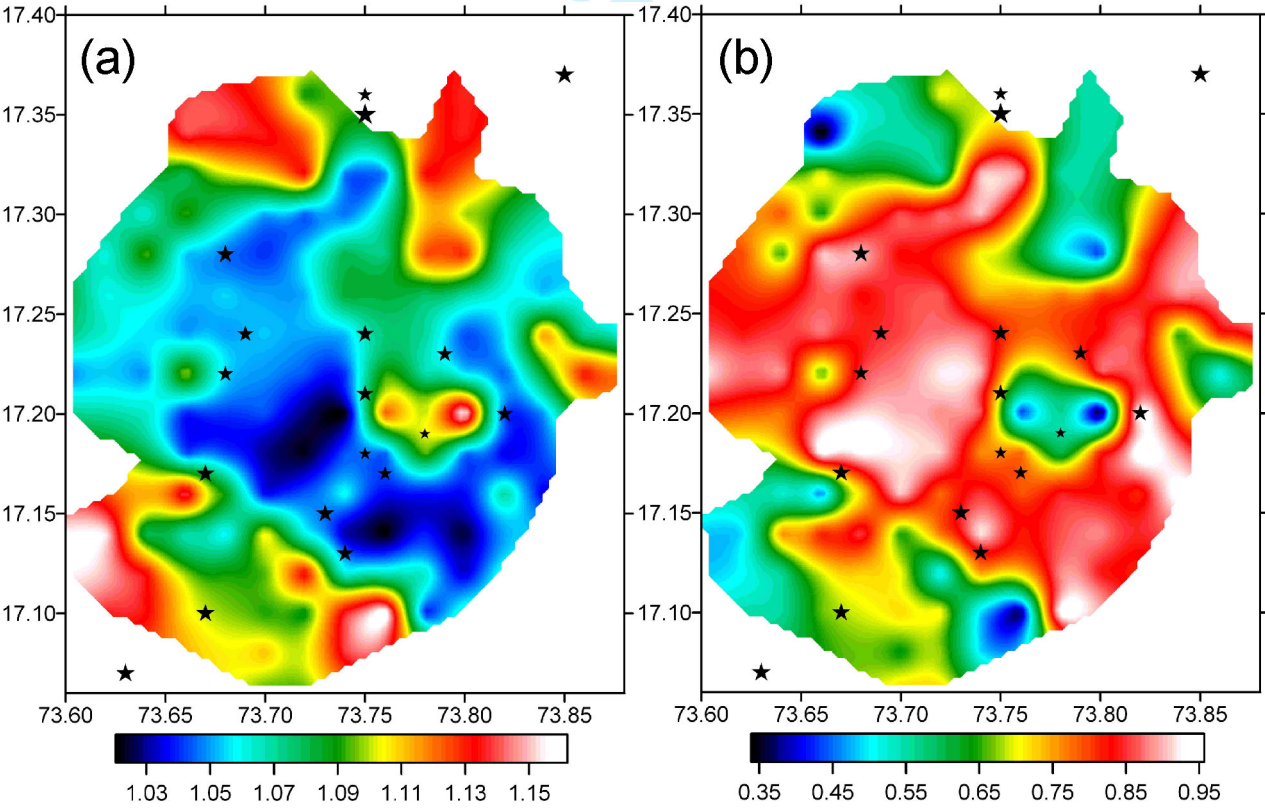


Figure 6